PCCP

Accepted Manuscript

ROYAL SOCIETY OF CHEMISTRY

www.rsc.org/pccp

Physical Chemistry Chemical Physics
CREATED USING THE RSC LaTeX PCCP ARTICLE TEMPLATE – SEE www.rsc.org/electronicfiles FOR DETAILS
ARTICLE TYPE www. rsc.org/xxxxxx | XXXXXXXX

Heat and Mass Transfer through Interfaces of Nanosized Bubbles/Droplets: the Influence of Interface Curvature

Øivind Wilhelmsen,*[a] Dick Bedeaux,[a] and Signe Kjelstrup[a]

Received Xth XXXXXXXXXX 20XX, Accepted Xth XXXXXXXXX 20XX
First published on the web Xth XXXXXXXXXX 200X
DOI: 10.1039/b000000x

Heat and mass transfer through interfaces is central in nucleation theory, nanotechnology and many other fields of research. Heat transfer in nanoparticle suspensions and nanoporous materials display significant and opposite correlations with particle and pore size. We investigate these effects further, for transfer of heat and mass across interfaces of bubbles and droplets with radii down to 2nm. We use square gradient theory at and beyond equilibrium to calculate interfacial resistances, in single-component and two-component systems. Interface resistances as defined by non-equilibrium thermodynamics, vary continuously with the interface curvature, from negative (bubbles) to zero (planar interface) to positive (droplet) values. The interface resistances of 2 nm radii bubbles/droplets are in some cases one order of magnitude different from those of the planar interface. The square gradient model predicts that the thermal interface resistances of droplets decrease with particle size, in accordance with results from the literature, only if the peak in the local resistivity is shifted toward the vapor phase. Curvature will then have the opposite effect on the resistance of bubbles and droplets. The model predicts that the coupling between heat and mass fluxes, when quantified as the heat of transfer of the interface, is of the same order of magnitude as the enthalpy change across the interface, and depends much less on curvature than the interface resistances.

1 INTRODUCTION

Boiling, condensation and crystallization are first order phase transitions at the core of a multitude of processes. Everyday examples can be found in refrigerators, bubbles in the soda, coffee machines and rain. In industry, phase transitions are central in transient operation of tanks and pipelines, chemical reactors and multiphase heat exchangers[1,2].

The field of nanotechnology is rapidly developing, and demands knowledge of phase transitions at the nanoscale. Self-assembly of nanoparticles at fluid interfaces (liquid-vapor and liquid-liquid) will for instance enable the preparation of high quality crystals, and nanoparticles at interfaces have been used to modify material stability[3,4]. The typical phase transition starts with the formation of a critical nanoscopic nucleus, which subsequently grows in size and combines with other entities to form a new phase[5]. The combined rate of these steps is the nucleation rate, which is crucial to properly describe the above processes. One of the reasons why nucleation is complicated, is that it is a non-equilibrium process[6], where the growth rate is decided by transfer of mass and energy. We know that the interface between the growing entities, the nanoparticles, and the surrounding fluid becomes important for small particles. Transfer of mass and energy will here depend strongly on the properties of the interface, as opposed to macroscopic systems where bulk effects dominate[7]. The growth process should thus be understood at the nanoscale, to correctly predict nucleation rates[8].

It is well known that the interface imposes additional resistance to transfer. This was noticed already in 1941 by Kapitza, in his observations of a temperature "jump" across a solid-liquid interface[9]. The interface resistance has later been quantified by kinetic gas theory (See[10] and refs. therein), non-equilibrium molecular dynamics (NEMD) simulations[11–13] and experiments[14,15]. The investigations with NEMD simulations report thermal resistances of the order 10^{-7}-10^{-8} m^{2}K/W for liquid-solid interfaces[16,17] and 10^{-10}-10^{-11} m^{2}K/W for vapor-liquid interfaces[11,13], which is much larger than in bulk systems. It is clear, also from experiments[18], that the interface is a barrier to transport. For a vapor-liquid interface with a thickness of 1 nm, the barrier has a magnitude equivalent to a μm thick gas layer according to kinetic gas theory[7].

Experiments have shown a dependence of the thermal conductivity in nanoparticle suspensions with the size of the particles, where the resistance decreases for smaller particles[19–21]. It was hypothesized by Lervik et al., that this was due to the interface curvature[12]. This was further demonstrated by the considerable radius dependence they predicted across a nanodroplet-water interface with NEMD-simulations[12]. It is very interesting that nanoporous materials exhibit the opposite behavior, where the resistance increases with smaller pores[22].

[a] *Department of Chemistry, University of Science and Technology, Trondheim, Norway; E-mail: oivind.wilhelmsen@ntnu.no*

In this work, we quantify and discuss the curvature dependence of interface resistances to heat and mass transfer, and also coupling effects between heat and mass. We investigate both single-component and two-component bubbles and droplets, i.e. vapor-liquid interfaces (also called surfaces). Interface resistances will be presented for bubbles/droplets with radii from 2 nm to the planar interface.

In our analysis, we use square gradient theory, both at and beyond equilibrium. Square gradient theory is the first approximation to density functional theory, first formulated for single-component systems by van der Waals[23], extended to mixtures by Cahn and Hillard[24] and to the non-equilibrium domain by Bedeaux and coworkers for single-component systems[25], and Glavatskiy and Bedeaux for mixtures[26]. The advantage of this model, compared to the capillary approximation in CNT[5,27,28], is that it provides continuous profiles through the interface and can be used to predict interface resistances. Prediction of interface resistances relies on local resistivity profiles and, as we shall see, assumptions about local resistivities affect interface properties strongly; curvature dependence in particular. Square gradient theory complements NEMD, Monte Carlo simulations and experiments, in that a comparison with these more sophisticated and time demanding approaches provides insight into the structure of the interface at the mesoscopic level[26].

We shall use equilibrium profiles combined with the integral relations to obtain interface resistances[29–31], and compare these to results from the non-equilibrium square gradient model, with actual gradients in temperature, composition and pressure[26,32]. We present interface resistances which vary continuously with the interface curvature, from negative (bubbles) to zero (planar interface) to positive (droplet) values. This has to the best of our knowledge, not been shown before. Moreover, we show that interface resistances are one order of magnitude different for 2 nm radii bubbles/droplets than for the planar interface, and that the peak in local resistivity must be shifted toward the vapor to give the expected curvature dependence of the thermal interface resistances of droplets. Curvature will then have the opposite effect on the resistance of bubbles, and give a behavior similar to that exhibited by nanoporous materials.

2 THEORY

We will in this section present the theoretical framework used. The equilibrium square gradient model was described previously[33]. We give the main equations in Sec. 2.1. The non-equilibrium formulation is discussed in Sec. 2.2. The different choices for local resistivities are described and justified in Sec. 2.3 before we discuss computational details in Sec. 2.4. How to go from the continuous description in the square gradient model, to a discontinuous description according to Gibbs' description is shown in Sec. 2.5. In particular, we discuss how to properly *calculate* excess properties from non-equilibrium profiles in curved systems (Sec. 2.5.1). We then repeat how to obtain interface resistance profiles from non-equilibrium profiles with the perturbation cell method[26,32] (Sec. 2.5.2), or from equilibrium profiles with the integral relations[29,30] (Sec. 2.5.3).

2.1 The equilibrium square gradient model

The equilibrium square gradient model represents a constrained stationary state of the system's Helmholtz energy (zero first functional derivatives), where the local Helmholtz energy density [J/m^3] depends on density and density gradients:

$$f_{\text{sgm}} = f_{\text{eos}} + \frac{1}{2}\sum_{ij=1}^{N_c} \kappa_{ij}\nabla\rho_i \cdot \nabla\rho_j \tag{1}$$

Here, i and j refer to the components, and N_c to the total number of components. Subscript sgm refers to the square gradient model, and eos to the local contribution. ρ_i is the density of component i, and κ_{ij} are the square gradient constants. If the mixing rule for the square gradient constants is defined according to the most common expression $\kappa_{ij} = \sqrt{\kappa_i\kappa_j}$, the differences between the square gradient, and the local chemical potentials become linearly dependent, and it is convenient to introduce the structure parameters κ, ε_i and q:

$$\kappa = \kappa_{N_c} \tag{2}$$

$$\varepsilon_i = \sqrt{\frac{\kappa_i}{\kappa}} \tag{3}$$

$$q = \sum_{i=1}^{N_c} \varepsilon_i\rho_i \tag{4}$$

Component N_c is chosen to be the most abundant one. All components are related through ε_i (note that $\varepsilon_{N_c} = 1$). We then obtain the thermodynamic quantities in terms of the structure parameters:

$$\mu_{\text{sgm},k} = \mu_{\text{eos},k} + \varepsilon_k\kappa\nabla^2 q \tag{5}$$

$$f_{\text{sgm}} = f_{\text{eos}} + \frac{\kappa}{2}(\nabla q)^2 \tag{6}$$

$$u_{\text{sgm}} = u_{\text{eos}} + \frac{\kappa}{2}(\nabla q)^2 \tag{7}$$

$$h_{\text{sgm}} = h_{\text{eos}} - \kappa q\nabla^2 q \tag{8}$$

$$p_{\text{sgm}} = p_{\text{eos}} - \frac{\kappa}{2}(\nabla q)^2 - \kappa q\nabla^2 q \tag{9}$$

Here, μ_k is the chemical potential of component k, u is the internal energy density, h the enthalpy density and p the pressure, which for the geometries considered here is parallel to the interface. The equilibrium square gradient model is thus

fully defined by the boundary conditions, a second order differential equation in q (Eq. 9), and (N_c-1) algebraic equations representing the linear dependence between thermodynamic quantities. We construct algebraic equations in terms of the chemical potential differences, $\Psi_k = \mu_k - \mu_{N_c}$:

$$\Psi_{\mathrm{eos},k} - \Psi_k = (\varepsilon_k - 1)\,\frac{\left(p_{\mathrm{eos}} - p_{sgm} - \frac{1}{2}\kappa(\nabla q)^2\right)}{q} \qquad (10)$$

Eq. 10 is a combination of Eq. 5 and 9, and is chosen for convenience. We could have used any set of (N_c-1) independent equations representing algebraic relations between the thermodynamic quantities, and obtained an equivalent model. In the remaining part of this work, thermodynamic quantities will always be defined according to the square gradient model. Furthermore, we divide Eqs. 6-8 by the overall density to have mass specific quantities and omit subscript sgm.

2.2 The non-equilibrium square gradient model

In the non-equilibrium square gradient model, we assume that thermodynamic quantities locally follow the same expressions as in equilibrium. Beyond equilibrium, there is transfer of heat and mass through the interface governed by conservation of mass, energy and momentum. The continuity equation is:

$$\frac{\partial \rho}{\partial t} = -\nabla\cdot(\rho\mathbf{v}) = -\nabla\cdot\mathbf{J} \qquad (11)$$

Here, $\mathbf{J}$ is the total mass flux which equals, $\rho\mathbf{v}$, where $\mathbf{v}$ is the barycentric velocity vector. The specie mass balances are:

$$\frac{\partial \rho_k}{\partial t} = -\nabla\cdot\left(\rho_k\mathbf{v} + \mathbf{J}_{d,k}\right) = -\nabla\cdot\mathbf{J}_k \qquad (12)$$

Where $\mathbf{J}_k$ is the mass flux and $\mathbf{J}_{d,k}$ is the diffusion flux of component k, with $\sum_{i=1}^{N_c}\mathbf{J}_{d,i} = 0$. The equation of motion is:

$$\frac{\partial(\rho\mathbf{v})}{\partial t} = -\nabla\cdot(\rho\mathbf{v}\mathbf{v}) - \nabla p - \nabla\cdot\gamma_{\alpha,\beta} \qquad (13)$$

We neglected the viscous stress tensor and external forces in the above equation. The symbol γ denotes the thermodynamic tension tensor, which has been derived for an interface described by the square gradient model assuming mechanical equilibrium[26,34]. With no external forces, it is:

$$\gamma_{\alpha,\beta} = \sum_{ij}^{N_c}\kappa_{ij}\frac{\partial\rho_i}{\partial x_\alpha}\frac{\partial\rho_j}{\partial x_\beta} = \kappa\left(\nabla_\alpha q\right)\left(\nabla_\beta q\right) \qquad (14)$$

Where α and β indicate the components of the coordinates. The total energy balance is:

$$\frac{\partial}{\partial t}\left(\rho\left(u + 0.5\mathrm{v}^2\right)\right) = -\nabla\cdot\left(\rho\mathbf{v}\left(u + 0.5\mathrm{v}^2\right) + \mathbf{J}_q + p\mathbf{v}\right) \qquad (15)$$

The Gibbs relation for the square gradient model was given by Glavatskiy[35]:

$$T\frac{ds}{dt} = \frac{du}{dt} - \sum_{i=1}^{N_c}\mu_i\frac{dw_i}{dt} + p\frac{d}{dt}\left(\frac{1}{\rho}\right) - (\mathbf{v}-\mathbf{v}_s)\,\frac{1}{\rho}\nabla\cdot\gamma \qquad (16)$$

Here, $d/dt \equiv \partial/\partial t + \mathbf{v}\cdot\nabla$ is the substantial time derivative, s the entropy, and w_i is the mass fraction of component i. Moreover, $\mathbf{v_s}$ is the velocity of the interface, which is zero in this work. The last term contributes only in the interfacial region. The entropy balance is:

$$\rho\frac{ds}{dt} = -\nabla\cdot\mathbf{J}_s + \sigma \qquad (17)$$

Here, $\mathbf{J}_s \equiv \mathbf{J}_{s,tot} - \rho s\mathbf{v}$ is the difference between the total entropy flux and the convective term $\rho s\mathbf{v}$, and σ denotes the local entropy production. Substituting for the balance equations in the Gibbs relation, the entropy flux and production are found to be[26]:

$$\mathbf{J_s} = \frac{1}{T}\left(\mathbf{J}_q - \sum_i^{N_c}\mu_i\mathbf{J}_{d,i}\right) = \frac{1}{T}\left(\mathbf{J}_q - \sum_i^{N_c-1}\Psi_i\mathbf{J}_{d,i}\right) \qquad (18)$$

$$\sigma = \mathbf{J}_q\cdot\nabla\left(\frac{1}{T}\right) - \sum_i^{N_c}\mathbf{J}_{d,i}\cdot\nabla\frac{\mu_i}{T} \qquad (19)$$

$$\sigma = \mathbf{J}_q\cdot\nabla\left(\frac{1}{T}\right) - \sum_i^{N_c-1}\mathbf{J}_{d,i}\cdot\nabla\frac{\Psi_i}{T} \qquad (20)$$

2.2.1 Phenomenological equations

The local entropy production in Eq. 20, consists of products of fluxes and thermodynamic forces, which according to classical non-equilibrium thermodynamics leads to the following linear force-flux relations from the first expression for σ:

$$\nabla\left(\frac{1}{T}\right) = r''_{qq}\mathbf{J}_q + \sum_i^{N_c} r''_{qi}\mathbf{J}_{d,i} \qquad (21)$$

$$-\nabla\left(\frac{\mu_k}{T}\right) = r''_{kq}\mathbf{J}_q + \sum_i^{N_c} r''_{ki}\mathbf{J}_{d,i} \quad k = 1,\ldots,N_c \qquad (22)$$

Or the equivalent, from the second expression for σ:

$$\nabla\left(\frac{1}{T}\right) = r_{qq}\mathbf{J}_q + \sum_i^{N_c-1} r_{qi}\mathbf{J}_{d,i} \qquad (23)$$

$$-\nabla\left(\frac{\Psi_k}{T}\right) = r_{kq}\mathbf{J}_q + \sum_i^{N_c-1} r_{ki}\mathbf{J}_{d,i} \quad k = 1,\ldots,N_c-1 \qquad (24)$$

Here, r'' and r are resistivity coefficients, which are expected to depend on both local variables and density gradients. The

linear form of these equations for interface transport has been verified by earlier work[36–38]. Furthermore, it can be remarked that distance from global equilibrium, is not in conflict with the existence of local equilibrium where thermodynamic relations are valid. Local equilibrium was verified for planar interfaces with similar gradients in temperature and composition as this work, using Gibbs excess variables[26,39]. With $\sum_i^{N_c} J_i = 0$, the relations between r'' and r become:

$$r_{qq} = r''_{qq} \quad (25)$$
$$r_{qi} = r_{iq} = r''_{iq} - r''_{N_c q} \quad (26)$$
$$r_{ki} = r_{ik} = (r''_{ki} - r''_{N_c i}) - (r''_{kN_c} - r''_{N_c N_c}) \quad (27)$$

We use Maxwell-Stefan's framework for multicomponent diffusion to define the bulk resistivities. The framework has many advantages, e.g. that it is independent of the frame of reference. The bulk the resistivity coefficients, r'' are identified as[7]:

$$r''^{\,o}_{qq} = \frac{1}{\lambda T^2} \quad (28)$$
$$r''^{\,o}_{qi} = r''^{\,o}_{iq} = -\left(h_i + q_i^{\,0}\right) r''^{\,o}_{qq} \quad (29)$$
$$r''^{\,o}_{ki} = r''^{\,o}_{ik} = -\frac{R}{c\text{Đ}_{ki} M_{w,i} M_{w,k}} + \frac{r''^{\,o}_{iq} r''^{\,o}_{kq}}{r''^{\,o}_{qq}} \quad (30)$$
$$r''^{\,o}_{kk} = d_k + \frac{(r''^{\,o}_{kq})^2}{r''^{\,o}_{qq}} \quad (31)$$

Here, superscript ^{o}, denotes values in the bulk phases. λ is the thermal conductivity, h_i is the partial mass enthalpy, $M_{w,i}$ the molar mass of component i, R the gas constant, c the total molar concentration and Đ_{ij} the Maxwell-Stefan diffusion coefficients. We used temperature and composition dependent models for the thermophysical properties, as described in Appendix A. With the same notation as[7], q_k^{o} is the local heat of transfer of component k on mass basis, and q_k^{o} and d_k are defined as:

$$q_k^{\,o} = \sum_{i\neq k}^{N_c} \frac{1}{M_{w,k}} \frac{RTx_i}{\text{Đ}_{ki}} \left(\frac{D_{T,k}}{\rho_k} - \frac{D_{T,i}}{\rho_i}\right) \quad (32)$$
$$d_k = \sum_{i\neq k}^{N_c} \frac{1}{M_{w,k}} \frac{Rx_i}{\text{Đ}_{ki}\rho_k} \quad (33)$$

Here, x_i is the mole fraction, and $D_{T,i}$ the thermal diffusion coefficient of component i.

2.3 Resistivities in the interfacial region

Across the interface, resistivities depend on gradients in densities in a way similar to what thermodynamic quantities do[33]. The exact nature of this dependence is yet unknown. We use the same dependence as recent literature and assume that local resistivity coefficients $r_j(x) = \left[r_{qq}, r_{q1}, r_{11}\right]$, are described by the following modulatory curves[26]:

$$r_{j,m} = r_j^g + (r_j^l - r_j^g) y_{\text{bulk}} + \alpha_{j,m} \left(r_j^g + r_j^l\right)_{eq,p} y_{\text{grad}} j_m \quad (34)$$

where:

$$y_{\text{bulk}} = \frac{\left(q - q^g_{\text{p,eq}}\right)}{\left(q^l_{\text{p,eq}} - q^g_{\text{p,eq}}\right)} \qquad y_{\text{grad}} = \frac{|q'|^2}{\left|q'_{\text{p,eq}}\right|^2_{max}} \quad (35)$$

Here, subscript "p,eq" means the equilibrium profiles from the planar interface. The first two terms on the right hand side of Eq. 34 represent a curve which follows the order parameter, q, from the gas bulk resistivities (superscript g), to the liquid bulk resistivities (superscript l). The above formulation differs in molar and mass units only by a constant, and behavior is thus independent of frame of reference. The term, y_{grad}, represents a contribution from the density gradients, similar to the contribution to the local Helmholtz energy in the square gradient model (see Eq. 6). The parameter α is a constant prefactor, which decides the amplitude of the gradient contribution. A contribution from density gradients in the expression for the thermal resistivity, r_{qq}, is strongly supported by the results from Holyst and Litniewksi[40]. They show that the temperature difference across the interface increases and the evaporation rate of nanodroplets decreases, the larger the difference in density becomes between the two phases. Gas et al. also discusses how diffusion is fundamentally different at the nanoscale[41].

NEMD simulations have indicated that the peak in the local resistivity profile is closer to the vapor-phase[11,42]. For some systems, however, the peak may be closer to the liquid-phase, so we consider three different cases for j_m with $m = \{1,2,3\}$:

$$j_1 = 1 \qquad j_2 = \left(\frac{q^l_{eq,p}}{q(x)}\right)^2 \qquad j_3 = \left(\frac{q(x)}{q^l_{eq,p}}\right)^2 \quad (36)$$

With j_1, the resistivity profile has no preference for the liquid or vapor-phase (Case n). With j_2, the peak in resistivity is closer to the gas-phase (Case g), and with j_3, the peak in resistivity is closer to the liquid-phase (Case l). Where possible, we chose the amplitude of the gradient term in the local resistivity profiles to reproduce interface resistances from kinetic gas theory with condensation coefficients set to 0.5. The values are given in Appendix B. In particular, α_{qq} was chosen to reproduce the thermal interface resistance, R_{qq}. The amplitudes of the cross coefficients, α_{q1} changed the interface resistances little and were set to 1.00. Values for mass transfer, α_{11}, were chosen to reproduce the interface resistance for mass of Component 2 from kinetic gas theory, R_{22}. This could not be achieved for the j_3-profile, and the $\alpha_{11,3}$-value was set to 1.00.

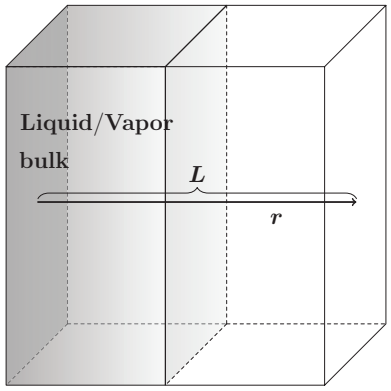

(a) Planar geometry

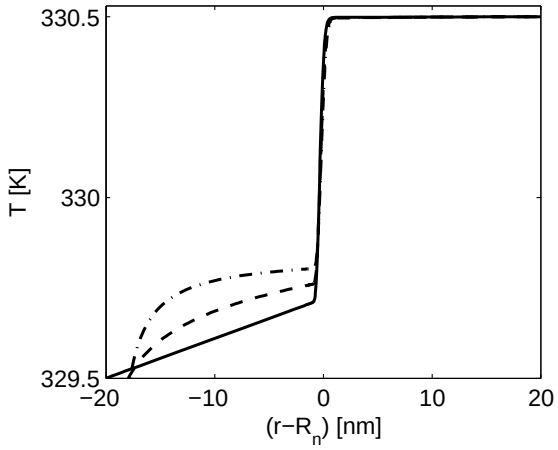

(b) Temperature profiles as functions of r

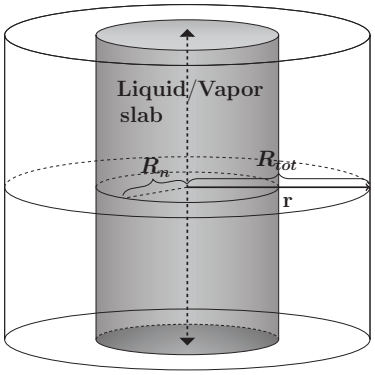

(c) Cylindrical geometry

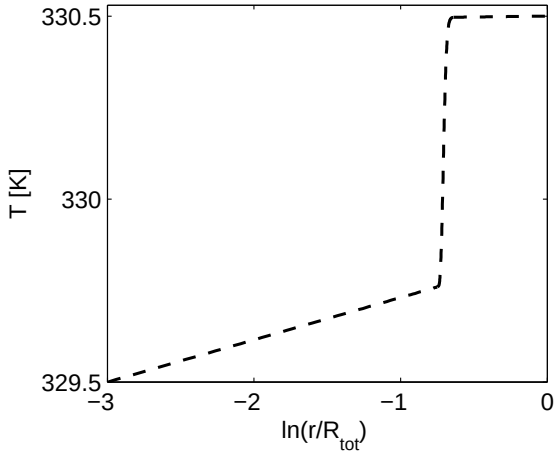

(d) Temperature profile through vapor slab

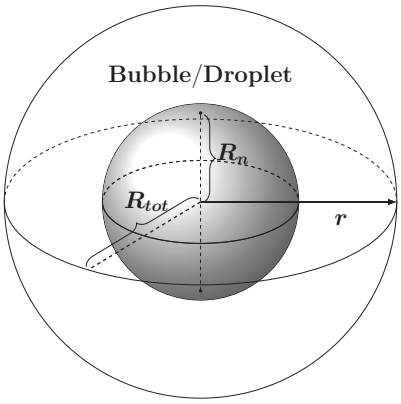

(e) Spherical geometry

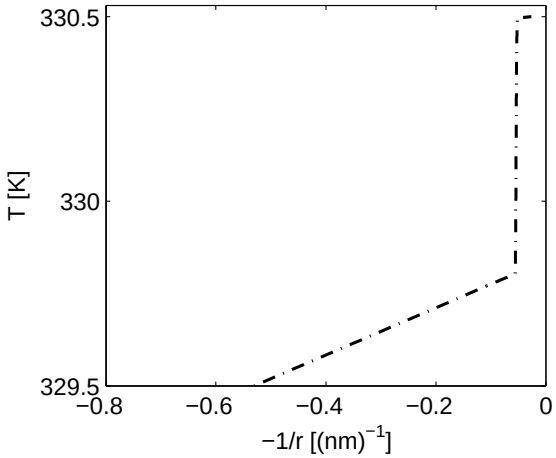

(f) Temperature profile through bubble

Fig. 1 Illustration of symmetric geometries (left) and temperature profiles (right) from the non-equilibrium square gradient model for a planar interface (solid line) a vapor slab (dashed line) and a bubble (dash-dot line) for the system hexane-cyclohexane.

Table 1 The balance equations at steady-state, the leading term for extrapolation and the Lam*é* coefficients of the symmetric geometries in Fig. 1

Geometry	Planar	Cylinder	Sphere
Momentum:	$\frac{(\partial J_m)}{\partial r} = 0$	$\frac{\partial (rJ_m)}{\partial r} = p$	$\frac{\partial \left(r^2 J_m\right)}{\partial r} = 2rp$
Mass:	$\frac{\partial (J_k)}{\partial r} = 0$	$\frac{\partial (rJ_k)}{\partial r} = 0$	$\frac{\partial \left(r^2 J_k\right)}{\partial r} = 0$
Energy:	$\frac{(\partial J_e)}{\partial r} = 0$	$\frac{\partial (rJ_e)}{\partial r} = 0$	$\frac{\partial \left(r^2 J_e\right)}{\partial r} = 0$
Leading term extrapolation:	r	$\ln(r)$	r^{-1}
Lam*é* coefficients:	$\mathfrak{h}_1 = \mathfrak{h}_2 = \mathfrak{h}_3 = 1$	$\mathfrak{h}_1 = \mathfrak{h}_2 = 1, \mathfrak{h}_3 = r$	$\mathfrak{h}_1 = 1, \mathfrak{h}_2 = r\sin(\theta), \mathfrak{h}_3 = r$

Kinetic theory applies to a system of hard spheres[7]. Transport properties predicted from the theory do not apply to real systems, as deviations from hard sphere values were found already for Lennard-Jones particles[43]. Since this work only aims to investigate qualitatively the curvature dependence of interface resistances, kinetic gas theory is sufficient as reference.

2.4 Solution method

For systems at steady-state with special symmetries, the square gradient model can be simplified considerably. These systems are; a planar interface, a cylinder, and a sphere, where the geometries are illustrated in Fig 1. In these cases the non-equilibrium square gradient model is reduced to a set of algebraic and one-dimensional first order differential equations. We define the momentum flux, J_m, and energy flux, J_e, as:

$$J_m = \rho \mathrm{v}^2 + \kappa (\nabla q)^2 + p \quad (37)$$

$$J_e = \rho \mathrm{v} \left(u + 0.5\mathrm{v}^2\right) + J_q + p\mathrm{v} \quad (38)$$

The balance equations can then be redefined according to the first rows of Tab. 1. Many of the equations are zero, meaning that the expressions in the parentheses are constant. Solving the balance equations is then reduced to a problem of finding a set of constants. This is more accurate and easier from a numerical point of view. The spherical geometry in Fig. 1e is the basis for our discussion of bubbles and droplets. In the non-equilibrium square gradient model, values of pressure, temperature and composition at boundaries are specified different from in the equilibrium configuration, which leads to a flux of energy and mass through the interface. For the curved interfaces in Figs. 1c and 1e, it is necessary to place the source/sink of mass and energy at a finite radius to avoid a diverging flux at $r = 0$. Non-equilibrium bubbles/droplets or cylinders configured according to the figures are never found at steady-state in nature, because the boundary conditions that sustain the fluxes across the interface are unrealistic. The models are, nonetheless, useful in the study of transport across curved interfaces, as we shall see in Sec. 3.

The combined system of differential and algebraic equations was solved using the "bvp4c" solver in Matlab, coupled with a multidimensional Newton-Raphson approach to solve the system of algebraic equations (Eq. 10) at each iteration. In the planar case, all balance equations were unknown constants, identified by the solver to satisfy the boundary conditions. In the curved cases, the momentum balance gave an additional differential equation to be solved. The scaled differential equations were solved to a relative accuracy of 10^{-8}.

2.5 From a continuous to discontinuous description

The square gradient model gives continuous profiles through the interface. According to Figs. 1b, 1d and 1f, the non-equilibrium square gradient model gives jumps in the temperature across the interface, which represents a barrier to transfer, such as observed in NEMD-simulations and experiments. In the study of macroscopic systems and nucleation processes, it is computationally demanding and unpractical to resolve the details of each bubble/droplet. One is then interested in the *overall* resistance to heat and mass imposed by the interface. This can be achieved by applying Gibbs' method for excess variables to R. From the calculation of the excess entropy production in Eq. 19 or 20 and the conditions at a steady-state interface, the linear force-flux relations can be defined with excess interfacial resistances, R. We refer to these for simplicity as interface resistances[26]. Subscript "n" is used to denote either a droplet or a bubble at the center of the container, and "e" for the exterior (see Fig.1f). The relation between thermodynamic forces and fluxes across the interface is then[7]:

$$\frac{1}{T^e} - \frac{1}{T^n} = R_{qq}J'^e_q + \sum_i^{N_c} R^e_{qi}J_i \quad (39)$$

$$-\left(\frac{\mu^e_k}{T^e} + \frac{\mu^n_k}{T^n}\right) - h^e_k\left(\frac{1}{T^e} - \frac{1}{T^n}\right) = R^e_{kq}J'^e_q + \sum_i^{N_c} R^e_{ki}J_i \quad (40)$$

Here, J'_q is the measurable heat flux, defined as: $J'_q = J_q - \sum_i^{N_c} h_i J_{d,i}$, and is independent of frame of reference. Note, that all quantities in Eq. 39 and 40 are bulk properties *extrapolated* from the phase indicated by the superscripts to the interface at radius, R_n. The above expressions differ from those defined in previous work, in that the vapor is not necessary located at the smaller spatial values (e.g. droplets and liquid slabs). Eqs. 39 and 40 use fluxes and enthalpies from the external phase as reference. They can also be defined in terms of the internal phase, and in this work, we present results only with the gas phase as reference. The above equations can be written more compactly as:

$$\mathbf{X} = \mathbf{RJ} \quad (41)$$

Here, $\mathbf{X}$ is a vector containing the thermodynamic forces, $\mathbf{R}$ a matrix with the interface resistances and $\mathbf{J}$ a vector with the fluxes from Eq. 39 and 40. We define the interfacial heat of transfer of component k as [J/kg]:

$$q^{*g,l}_k = \left(\frac{J'^{\,g,l}_q}{J_k}\right)_{\Delta T=0, J_{i\neq k}=0} = -\frac{R^{g,l}_{qk}}{R_{qq}} \quad (42)$$

q^*_k is defined in terms of the measurable heat flux. The heats of transfer, also called heat of transport, can be defined either with respect to the gas phase, or with respect to the liquid phase. The following relation has been derived by Kjelstrup and Bedeaux[7]:

$$q^{*g}_k - q^{*l}_k = -\Delta_{g,l}h_k \quad (43)$$

Where, $\Delta_{g,l}h_k$, is the change in partial mass enthalpies of component k across the interface, which for single-component systems is known as the vaporization enthalpy. Eq. 43 shows that some of the coupling coefficients between mass and energy across the interface must be of the same order of magnitude as the enthalpy difference across the interface, i.e. much larger than in bulk systems. We shall discuss this quantity in more detail in Sec. 3.

Physically feasible local resistivity profiles must result in a positive excess entropy production. The interface resistance matrix, $\mathbf{R}$, must therefore be positive definite. To achieve this, the main coefficients R_{qq}, R_{11} and R_{22}, must be positive. The cross coefficients, R_{12}, R_{q1} and R_{q2}, however, are allowed to be negative, if the following inequality is satisfied for every $z = \{i \neq k, q\}$:

$$0 < R_{kk}R_{zz} - R^2_{zk} \quad (44)$$

2.5.1 Excess properties of curved interfaces

To properly define excess properties from non-equilibrium profiles, state variables must be extrapolated to the interfacial region from the bulk phases. How to do this for planar interfaces was discussed in detail by Johannessen and Bedeaux[39], where state variables were fitted to polynomials in the spatial variable, r, in bulk regions. It is evident from Fig. 1b why this is an excellent idea, since temperatures are close to linear in the bulk phases, even if the mixture has highly non-linear thermophysical properties. Curved systems do not give temperature profiles which are linear in r according to the dashed and the dash-dot lines in Fig. 1b. In fact, there are no polynomials with r as argument which give satisfactory extrapolation in the cylindrical and spherical geometries (Fig 1c and 1e).

A cylindrical geometry gives temperature profiles which are nearly linear in $\ln(r)$ according to Fig. 1d, and a spherical geometry gives profiles which are nearly linear in r^{-1} according to Fig. 1f. This is because temperature profiles in the bulk-phases are well approximated by the equation for steady-state heat conduction, the Laplace equation. The spatial variables suitable for extrapolation in the geometries considered in this work are summarized in Tab. 1.

2.5.2 The perturbation cell method

The idea behind the perturbation cell method is to solve the non-equilibrium square gradient model with small perturbations from equilibrium. The responding fluxes and thermodynamic forces will then represent the linear response, and can be used to find interface resistances. The interface resistance matrix can be estimated using:

$$\mathbf{R} = \mathbf{X}\mathbf{J}^T \left(\mathbf{J}\mathbf{J}^T\right)^{-1} \tag{45}$$

This equation gives the least square value of **R** given **J** and **X**. To estimate the matrix of interface resistances to a sufficient accuracy requires a number of independent perturbations which exceeds the number of independent interface resistances. We used $(4+2N_c)$ perturbations, specified as in literature[26,32]. We refer to the work by Johannessen and Bedeaux for further discussion of the perturbation cell method[32].

2.5.3 The integral relations

The integral relations were discussed for single components systems and planar interfaces by Johannessen and Bedeaux[29] and extended to mixtures and systems with curvature by Glavatskiy and Bedeaux[30]. They introduced the operator $\mathfrak{E}_r$, defined as:

$$\mathfrak{E}_r\{\phi\} = \mathfrak{h}_2^s \mathfrak{h}_3^s \int_{r_{s,-}}^{r_{s,+}} dx_1 \frac{\mathfrak{h}_1}{\mathfrak{h}_2\mathfrak{h}_3}\phi^{ex} \tag{46}$$

Here, the region from $r_{s,-}$ to $r_{s,+}$ represents the interfacial region, and $\mathfrak{h}_1, \mathfrak{h}_2, \mathfrak{h}_3$ are the Lam*é*-coefficients (see Tab. 1). For single-component systems the interface resistances were found to be:

$$R^g_{qq} = \mathfrak{E}_r\{r_{qq}\} \tag{47}$$
$$R^g_{q1} = \mathfrak{E}_r\{r_{qq}(h^g - h)\} \tag{48}$$
$$R^g_{11} = \mathfrak{E}_r\left\{r_{qq}(h^g - h)^2\right\} \tag{49}$$

And for a two-component system:

$$R^g_{qq} = \mathfrak{E}_r\{r_{qq}\} \tag{50}$$
$$R^g_{q1} = \mathfrak{E}_r\{-r_{qq}(h - h_1^g) + r_{q1}w_2\} \tag{51}$$
$$R^g_{q2} = \mathfrak{E}_r\{-r_{qq}(h - h_2^g) - r_{q1}w_1\} \tag{52}$$
$$R^g_{11} = \mathfrak{E}_r\left\{r_{qq}(h - h_1^g)^2 - 2r_{q1}w_2(h - h_1^g) + r_{11}w_2^2\right\} \tag{53}$$
$$R^g_{12} = \mathfrak{E}_r\{r_{qq}(h - h_1^g)(h - h_2^g) + r_{q1}(w_1(h - h_1^g) - w_2(h - h_2^g)) - r_{11}w_1w_2\} \tag{54}$$
$$R^g_{22} = \mathfrak{E}_r\left\{r_{qq}(h - h_2^g)^2 + 2r_{q1}w_1(h - h_2^g) + r_{11}w_1^2\right\} \tag{55}$$

For multicomponent systems, the expressions are more complicated, but can be elaborated based on Chapter 8 in[26], which we refer to for further details and derivations.

3 RESULTS AND DISCUSSION

The formalism in Sec. 2 was presented for multicomponent systems. For simplicity, however, results will be particularized for the single-component system hexane, and the binary system, cyclohexane-hexane (Component 1-2) at 330K because they have been popular in literature[13,26]. In previous work, we presented stationary solutions of the square gradient model for a two-component system with a fixed overall composition[33]. In this work, we use a fixed composition in the external phase. This is a more natural boundary condition with a clear physical interpretation, because it gives bubbles/droplets nucleating in the same mixture, and extrapolate to the same state at zero curvature. In particular, the composition in the external phase corresponds to the coexistence state at 330K and 0.5981 bar. The phase envelope and stability with these conditions are qualitatively the same as with constant overall composition (See Fig. 4 in[33]). Parameters and scales associated with the square gradient model are the same as in previous work[33]. In Sec. 3, we first compare the two methods presented to find interface resistances, namely the perturbation cell method and the integral relations (Sec. 3.1), before we proceed to discuss interface resistances of bubbles/droplets with radii from 2 nm to the planar interface (Sec. 3.2). We associate bubbles with negative and droplets with positive curvatures according to standard convention (curvature with respect to the liquid phase).

We use the same container radius, $R_{\text{tot}} = 37.7$nm, in all simulations (See Fig. 1e). If the size of the container for a given bubble/droplet size is increased, keeping the density and composition in the outer phase constant, we find that the description of the bubble/droplet and also the interface resistances do not change. Interface resistances are found to be independent of container size, however, the bubble/droplet becomes unstable in larger containers. We refer to Sec. 3.3 for a discussion of this, were we conclude that it makes perfect sense to calculate interface resistances also for unstable bubbles/droplets, given that there is no essential change in the description of the bubble/droplet.

3.1 The integral relations and the perturbation approach

Fig. 2 shows a comparison of interface resistances calculated with the integral relations (lines), and with the perturbation cell method (stars). The two methods predict the same interface resistances within a sufficient accuracy (<0.1%). We present the heat-mass cross resistance for the single-component system (Fig. 2a), and the thermal interface resistance for the two-component system (Fig. 2b), but could well have chosen any other two interface resistances to demonstrate that the methods give the same results.

We thus confirmed numerically that the integral relations derived by Bedeaux and coworkers are valid, also for multi-component systems with curvature. Moreover, Fig. 2 gives credibility to our implementation, and to the numerical accuracy chosen. From a practical point of view, we recommend the integral relations to calculate interface resistances, in particular for curved systems. The first reason for this is the placement of the source/sink of mass and energy at a finite radius in the spherical container, which makes the perturbation method inaccurate for small bubbles/droplets (radii below 5nm). Furthermore, the difference in computational time is considerable. The time needed to calculate equilibrium profiles and compute the integral relations is in the order of seconds. The perturbation cell method needs 6 and 8 solutions of the non-equilibrium square gradient model for the single-component and the two-component systems respectively, which gives a calculation time of approximately 15 minutes for every star in Fig. 2a, and about 1 hour for every star in Fig. 2b. Consequently, we used the integral relations to calculate the interface resistances in the remaining part of this work.

3.2 Interface resistances

Figs. 3, 4 and 5 show how interface resistances change from bubbles with 2nm radius (negative curvature) to the planar interface with zero curvature to 2nm droplets (positive curvature). We present results based on gas-phase enthalpies and fluxes, but have also calculated interface resistances based on the liquid phase. Moreover, we have checked that all presented interface resistances give positive definite resistance matrices, i.e. that Eq. 44 is satisfied. Even if some of the cross-coefficients are negative, they are in agreement with the second law of thermodynamics.

The results presented refer to the radii defined by the equimolar dividing interface of the total molar density. We also calculated interface resistances with radii corresponding to the interface of tension. This gave slightly different absolute values of the interface resistances, but we confirmed that they had the same curvature dependence. For the cases examined, the curvature dependence is qualitatively independent of the choice of dividing interface. This agrees with recent work by Glavatskiy and Bedeaux examining bubbles with radii above 20nm. They showed that there was little difference between the interface resistances with three choices of the dividing interface [31].

Resistances both for one- and two-component systems vary continuously with the interface curvature, from negative (bubbles) to zero (planar interfaces) to positive (droplet) values. For one component, also the first derivatives of the interface resistances are continuous. This emphasizes the symmetric and connected nature of bubbles and droplets, discussed earlier [33]. In the two-component case, we found that only the first derivative for the thermal interface resistance, R_{qq}, was continuous. The observed discontinuity of the first derivative in the other resistances is a consequence of the fact that the composition in the external phase is fixed. The external phase, and hence the external composition changes discontinuously in $(R_n^{-1} = 0)$.

A common property of all figures is that the curvature dependence of the interface resistances is closely connected to the nature of the local resistivities. As explained in Sec. 2.3, three different local resistivity functions were considered; one neutral (Case n), one with the peak closer to the gas-phase (Case g), and one with the peak closer to the liquid-phase (Case l). With freedom to choose amplitudes of the gradient contributions, we chose kinetic gas theory as reference for the thermal interface resistance, R_{qq}, at the planar interface. The same reference was used for the mass interface resistance of component 2, R_{22}, in the two-component case (see Sec. 2.3 for details). Consequently, the profiles in Figs 3 and 4b cross the vertical-axis in the same point. Even if the local resistivity profiles give the same interface resistances for a planar interface, they give very different predictions for small bubbles and droplets. In Case n, interface resistances depend only moderately on the radii of the bubbles/droplets (typically <10%). A shift in the position of the peak in local resistivity, however, will give significant curvature dependence. Consider for instance Fig. 3, or Fig. 4b, where interface resistances given by the dashed lines (Case g) are one order of magnitude higher for the smallest bubbles than at the planar interface.

For all interface resistances, except R_{12} and R_{q2} in the two-component case, a shift of the peak toward the vapor-phase or the liquid-phase has the opposite effect on curvature dependence. Molecular dynamics simulations and experiments indicate that thermal resistance of droplets, R_{qq}, should decrease with smaller particles, i.e. give a better thermal conductance [12,19,20]. This behavior is only exhibited by Case g in Fig. 3, where the peak in local resistivities is shifted toward the vapor-phase. A peak closer to the vapor-phase is actually consistent with NEMD-simulations, see for instance Fig. 4 in [11]. Amazingly, square gradient theory predicts qualitatively reasonable curvature dependence for the thermal interface resistance of droplets, but only with a local resistivity similar to that from NEMD-simulations. Even if curvature appears to enhance transport of mass and energy across interfaces of droplets, the square gradient model predicts the opposite effect on bubbles according to the dashed lines in Fig 3. We have not succeeded to find any simulations or experiments which elaborate further on this. However, we believe it can help explain why the thermal conductivity decreases with pore size in nanoporous materials [22], when the opposite effect is observed in nanoparticle suspensions [12]. In the pores, the

density is much lower than in the surrounding substance, similar to the situation for bubbles in a liquid.

The thermal interface resistances are very similar for one and two components (Fig. 3a and 3b), but this is not the case for the rest of the resistances. The resistance to mass-transfer of hexane, for instance, is different both in magnitude and behavior (compare R_{22} values in Fig. 4a and 4b). While the liquid-gas phase transition in a single-component system is purely evaporation/condensation, the picture is much more complicated with two components. In multicomponent systems, also a separation of components should be expected at the interface, meaning that components move in opposite directions. The common property of the curvature dependence is that the main coefficients, R_{11} and R_{22} depend on curvature similar to the thermal interface resistance, i.e. transfer is enhanced for droplets and diminished for bubbles at smaller radii in Case g. The cross coefficient R_{12} has a different behavior, but is of the same order of magnitude as the main coefficients. The above discussion shows that one should not use interface resistances calculated for single-components in multicomponent systems.

The cross coefficients between heat and mass, R_{q1} and R_{q2} presented in Fig. 5, are best discussed in terms of the heats of transfer of the interface, shown in Fig. 6. The heats of transfer were calculated with Eq. 42, which we have divided by the difference in partial mass enthalpies across the interface. We verified that all profiles presented satisfy Eq. 43. A first observation is that enthalpy differences across the interface and heats of transfer are comparable in size, and the heat of transfer of Component 2 is actually larger than the difference in partial mass enthalpy for Cases n and l (Fig. 6b). In other words, the mass flux during evaporation at constant temperature, carries an amount of heat to the interface which is larger than the enthalpy of evaporation[44]. The excess heat is carried into the next phase with the mass flux. A similar magnitude of the heat of transfer was observed by Inzoli et al. using NEMD-simulations[13].

The coupling between heat and mass across the interface is 7 orders of magnitude larger than in the bulk region of the gas-phase! The large value means that all consistent modeling of heat and mass across interfaces must take the coupling effect into account. This is not yet generally apprehended in the engineering society[2]. The figures show that the heats of transfer across the interface depend much less on curvature than the interface resistances. In previous work, they were also found to be insensitive to large changes in the pressure[44].

Figures and discussion in Sec. 3 show that square gradient theory can predict how interface resistances change with size of bubbles/droplets, *given* that we know the behavior of local resistivities. NEMD-simulations have shown that the local resistivities have peaks closer to the vapor-phase, and that they are larger in the interfacial region than in the bulk phases[11,42]. Apart from that, further details about functional forms of the local resistivities are currently unknown. We thus recommend that these effects should be quantified by NEMD-simulations which determine the local resistivities and compare with results from square gradient theory to give insight into the local structure of interfaces. This will in the future facilitate further comparison with e.g. state-of-the-art NEMD-simulations of droplet evaporation[40,45].

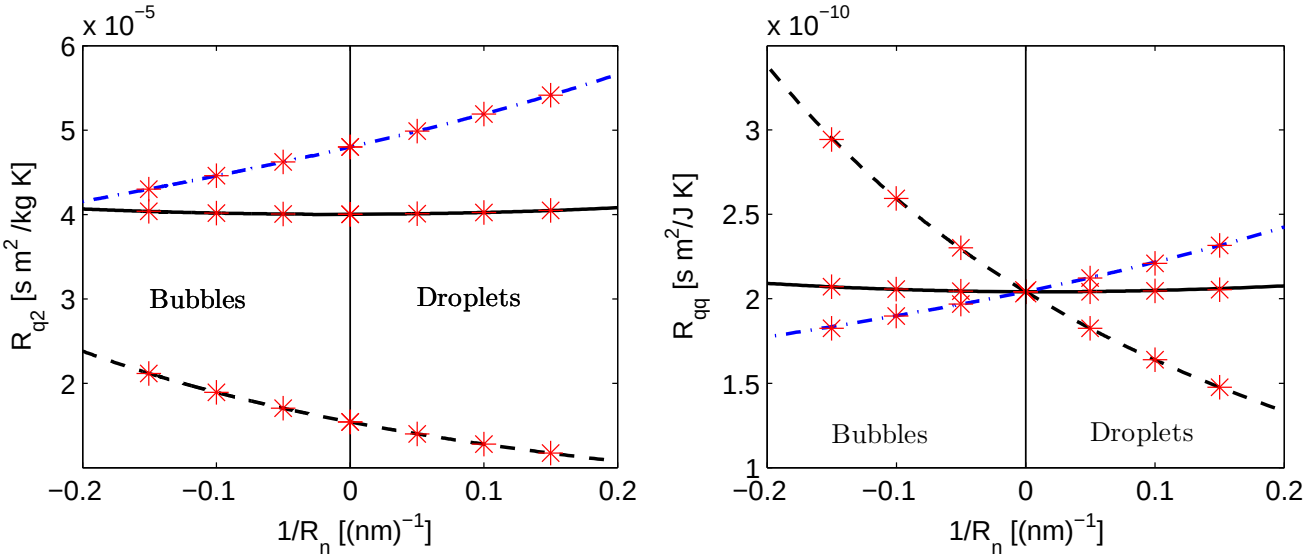

(a) Hexane **(b)** Hexane-cyclohexane

Fig. 2 Heat-mass cross coefficients in the single-component system (left) and thermal interface resistance coefficients in the two-component system (right). Case n (solid line), Case g (dashed line) and Case l (dash-dot line). The stars are results from the perturbation cell method.

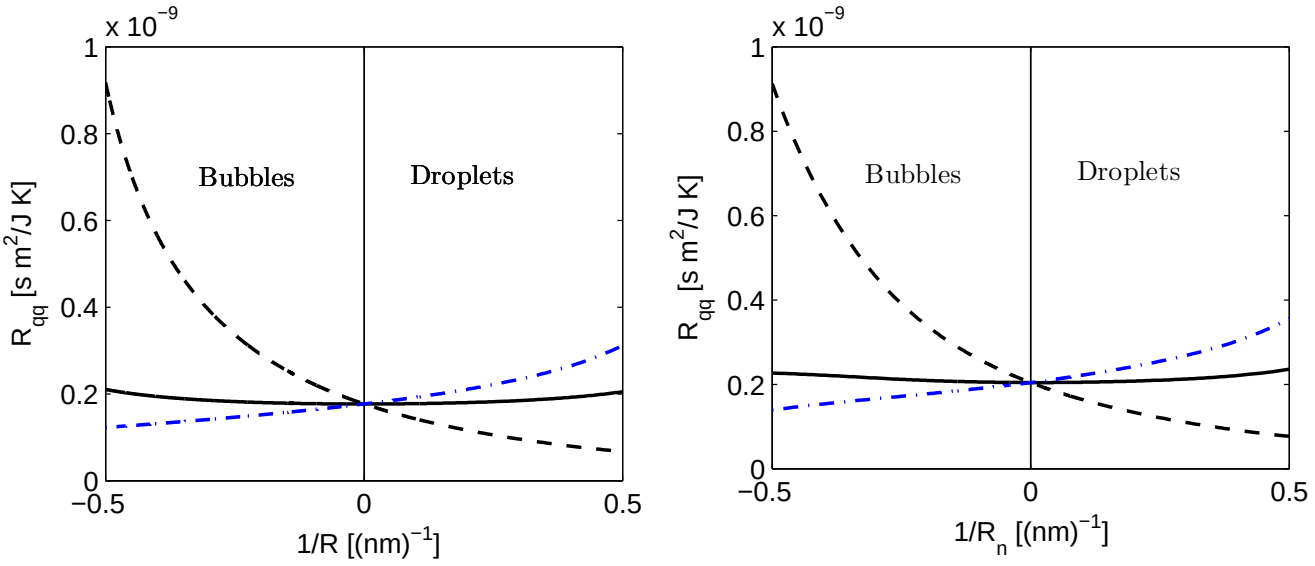

(a) hexane **(b)** hexane-cyclohexane

Fig. 3 Thermal interface resistance coefficients. Case n (solid line), Case g (dashed line) and Case l (dash-dot line).

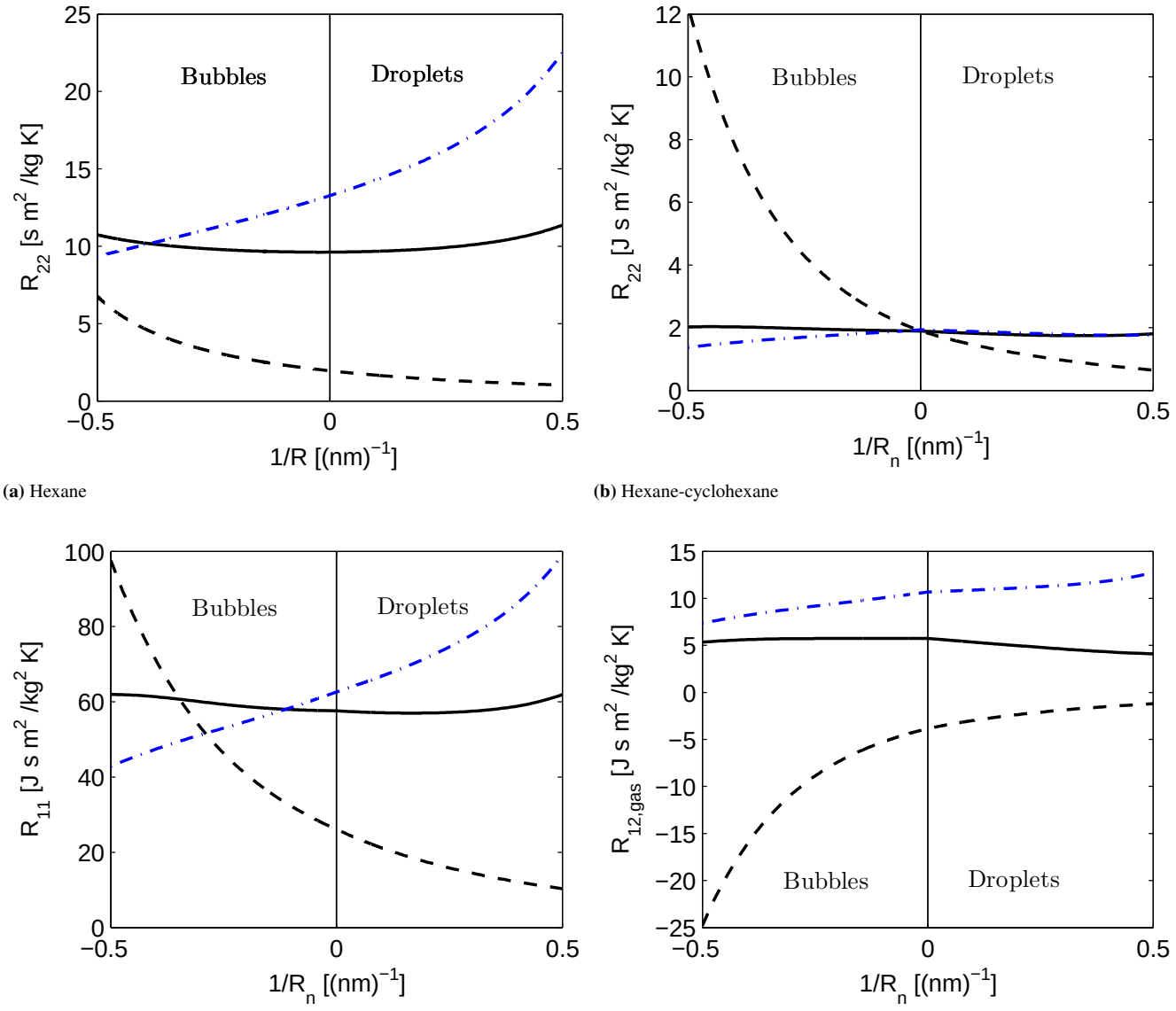

(a) Hexane

(b) Hexane-cyclohexane

(c) Hexane-cyclohexane

(d) Hexane-cyclohexane

Fig. 4 Interface resistance coefficients for mass. Case n (solid line), Case g (dashed line) and Case l (dash-dot line).

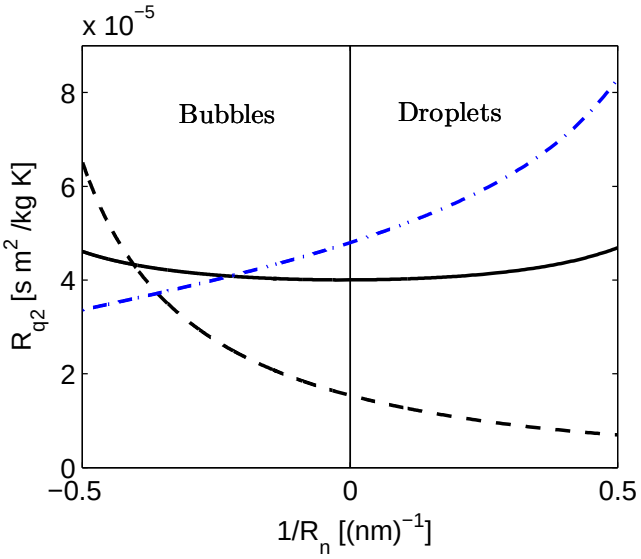

(a) Hexane

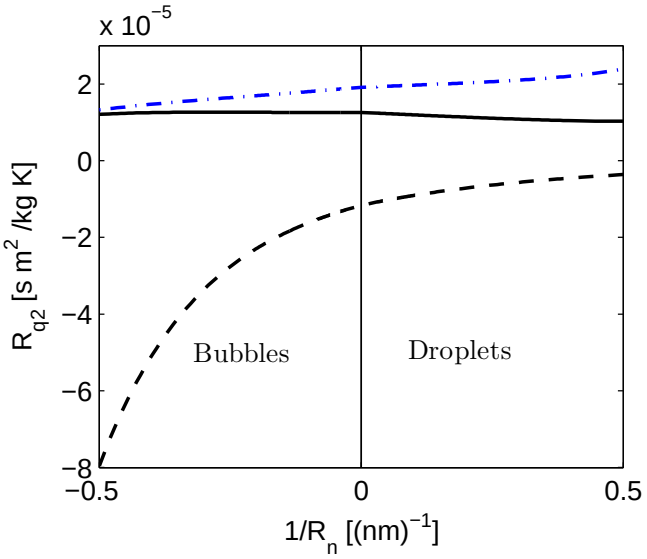

(b) Hexane-cyclohexane

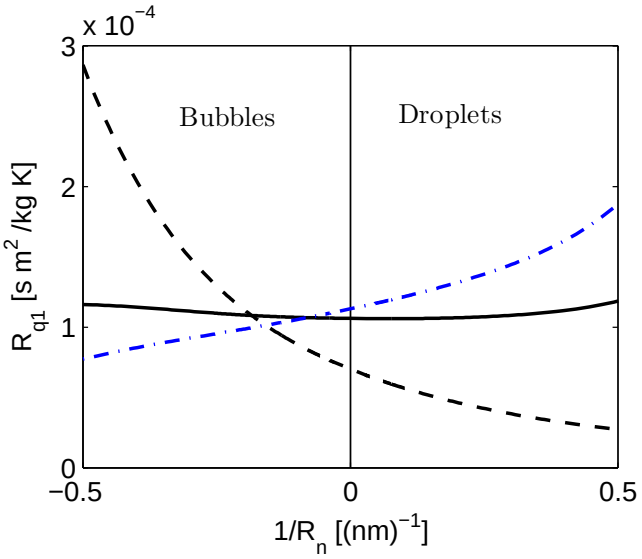

(c) Hexane-cyclohexane

Fig. 5 Interface resistance heat-mass cross coefficients. Case n (solid line), Case g (dashed line) and Case l (dash-dot line).

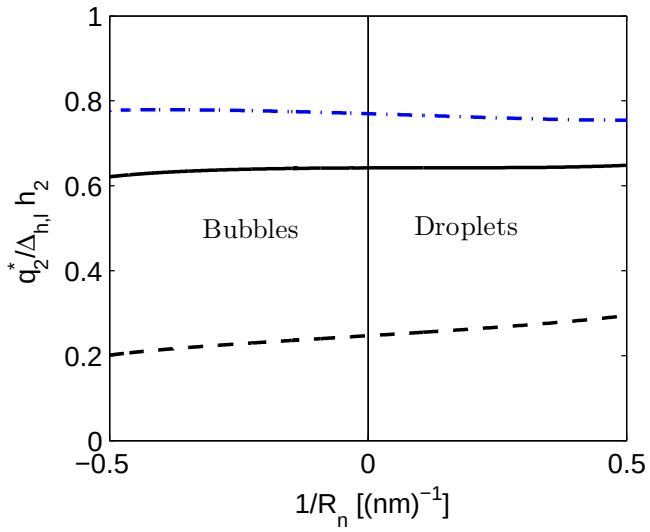

(a) Hexane

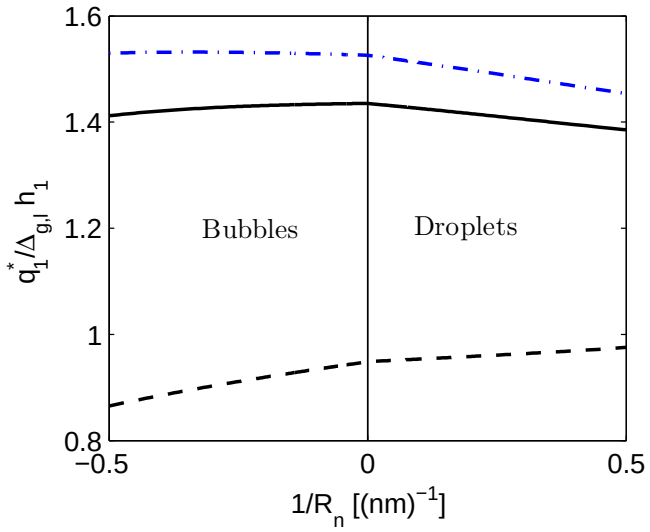

(b) Hexane-cyclohexane

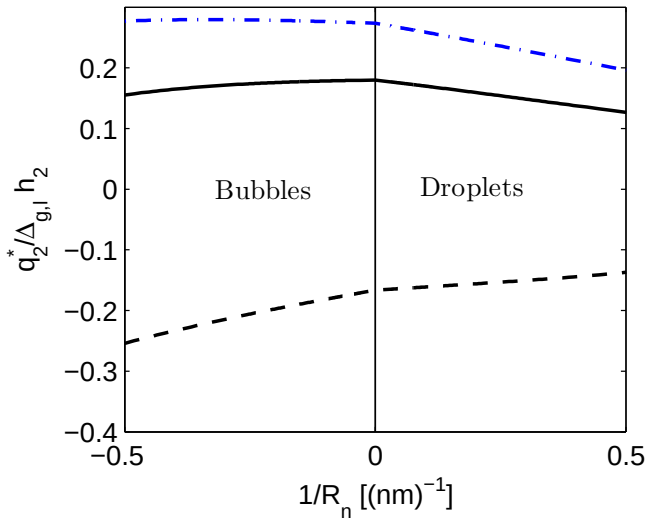

(c) Hexane-cyclohexane

Fig. 6 Heats of transfer divided by partial mass enthalpies. Case n (solid line), Case g (dashed line) and Case l (dash-dot line)

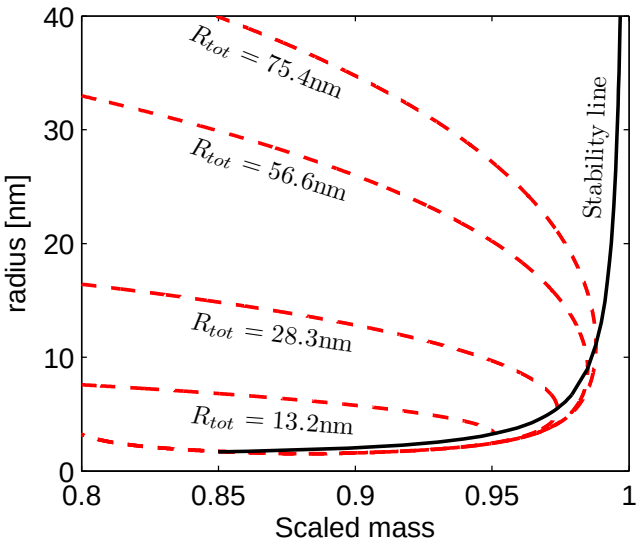

Fig. 7 Bubble radius as function of scaled mass in the container, with four different total radii of the container (red dashed lines). The thermodynamic stability limit with changing container size (solid line)

3.3 Transfer coefficients and thermodynamic stability

Bubbles and droplets are intrinsically unstable in atmospheric conditions (constant temperature and pressure), however, they can be stabilized in closed systems[46]. We have presented interface resistances for bubbles and droplets with radii down to 2nm, where the smallest bubbles/droplets are thermodynamically unstable with the given container size. In Fig. 7, the upper branches of the dashed lines correspond to stable bubbles, which turn into unstable bubbles at the lower branches. The scaled mass is the total mass in the system divided by the mass in a container filled with the liquid-phase at coexistence conditions. The figure shows that the minimal size of stable bubbles/droplets depends strongly on the total container volume. Smaller container volumes enable smaller bubbles and droplets to be conserved, where the state of the smallest possible bubble follows the solid line. Bubbles/droplets can be stabilized down to a minimum radius located at the bottom of the curves.

Only solutions of the square gradient model which correspond to minima of the Helmholtz energy are thermodynamically stable, and represent steady-state bubbles/droplets. In theory, one could calculate interface resistances from stable bubbles/droplets using a range of container volumes as illustrated by the dashed lines in Fig. 7. The analysis can be simplified by realizing that the description of the bubble/droplet is independent of container size. This is true if the surface energy of the container wall is negligible. Bubbles/droplets which can be stabilized in *some* container are identical to stationary solutions representing unstable bubbles/droplets in larger containers, and it is only necessary to consider results from one container volume. In the capillary description from CNT, this can be proven rigorously. At equilibrium, all intensive variables describing the bubble/droplet are in this description uniquely determined by the temperature, radius, density and composition in the outer phase. It is then always possible to make the bubble/droplet thermodynamically unstable by increasing the container size, and adding mass to keep density and composition in the outer phase fixed. The bubble/droplet, however, remains unchanged. With solutions from the square gradient model, this can only be shown numerically. We have thus investigated the stationary solutions of the square gradient model with changing container size and indeed verified that the properties of the bubble/droplet are independent of the container size, if $R_n \ll R_{\text{tot}}$. In particular, the interface resistances as function of radius remained the same.

4 CONCLUSION

We have investigated how transport of heat and mass across the interface depends on the curvature of bubbles and droplets. Overall interface resistances were presented for both single-component and two-component systems. They were obtained most accurately with integral relations, based on solutions from the equilibrium square gradient model. We verified that the non-equilibrium square gradient model with gradients in temperature, pressure and composition gave the same results. The interface resistances varied continuously with the interface curvature, from negative (bubbles) to zero (planar interface) to positive (droplet) values. In some cases, interface resistances changed one order of magnitude from the planar interface to 2 nm radii bubbles/droplets. If the peak in local resistivity was shifted toward the vapor-phase, the square gradient model predicted the thermal interface resistances of droplets to decrease with particle size, in accordance with results from the literature. Curvature had then the opposite effect on bubbles than droplets, and exhibited behavior similar to that found in nanoporous materials. The interface resistances were found to be independent of the container size used in the simulations. Heats of transfer of the interface were of the same order of magnitude as the enthalpy difference across the interface, and depended much less on curvature than the interface resistances. The heat-mass coupling resistances must thus be taken into account for accurate modeling of transport across interfaces. We recommend future comparison with NEMD-simulations to further quantify the curvature effects.

AKNOWLEDGEMENTS

Øivind Wilhelmsen would like to thank the Faculty of Natural Sciences and Technology at the Norwegian University of Science and Technology for the PhD-grant. We thank Prof. D. Reguera for fruitful discussions.

References

1 Wilhelmsen Ø. Skaugen G. Hammer M. Wahl P.E. Morud J.C., *Ind. Eng. Chem. Res.*, 2013, **52(5)**, 2130.
2 Aursand P. Hammer M. Munkejord S.T. Wilhelmsen Ø, *Int. J. Greenhouse Gas Control*, 2013, **15**, 174.
3 Lin Y. Böker A. Skaff H. Cookson D. Dinsmore A.D. Emrick T. Russel T.P., *Langmuir*, 2005, **21(1)**, 191.
4 Bresme F. Oettel M., *J. Phys: Condends. Matter*, 2007, **19**, 413101.
5 H. Vehkamäki, *Classical Nucleation Theory in Multicomponent Systems*, Springer, 2006.
6 Reguera D., *J. Non-Equilibrium Thermodynamics*, 2005, **29(4)**, 327.
7 Kjelstrup S. Bedeaux D., *Non-equilibrium Thermodynamics of Heterogeneous Systems*, World-Scientific, 2008.
8 Li T. Donadio D. Galli G., *Nature communications*, 2013, **4**, 1887.
9 Kapitza P.L., *J. Phys.*, 1941, **4**, 181.
10 Bedeaux D. Hermans L.J.F. Ytrehus T., *Physica A*, 1990, **169**, 263.
11 Simon S.M. Bedeaux D. Kjelstrup S. Xu J. Johannessen E., *J. Phys. Chem. B*, 2006, **110(37)**, 18528.
12 Lervik A. Bresme F. Kjelstrup S., *Soft Matter*, 2009, **5**, 2407.
13 Inzoli I., Kjelstrup S. Bedeaux D. Simon J.M., *Chem. Eng. Sci.*, 2011, **66(20)**, 4533.
14 Fang G. Ward C.A., *Phys. Rev. E*, 1999, **59(1)**, 417.
15 Ward C.A. Stanga D., *Phys. Rev. E*, 2001, **64**, 051509.
16 Patel H.A. Garde S. Keblinski P., *Nano Lett.*, 2005, **5(11)**, 2225.
17 Zhenbin G. Cahill D.G. Braun P.V., *Phys. Rev. Lett.*, 2006, **96(18)**, 186101.
18 Smith J.D. Cappa C.D. Drisdell W.S. Cohen R.C. Saykally R.J., *JACS*, 2006, **128**, 12892.
19 Keblinski P. Phillpot S.R. Choi S.U.S. Eastman J.A., *Int. J. of Heat and Mass Transfer*, 2002, **45(4)**, 855.
20 Patel H.E. Das S.K. Sundararajan T. Nair A.S. George B. Pradeep T., *Appl. Phys. Lett.*, 2003, **83**, 2931.
21 Hu M. Poulikakos D. Grigoropoulos C.P Pan H., *J. Chem. Phys.*, 2010, **132(16)**, 164504.
22 Bera C. Mingo N. Volz S., *Phys. Rev. Lett.*, 2010, **104**, 115502.
23 Rowlinson J.S., *Journal of Statistical Physics*, 1979, **20(2)**, 197.
24 Cahn J.W. Hillard J.E., *J. Chem. Phys.*, 1958, **28(2)**, 258.
25 Bedeaux D. Johannessen E. Røsjorde A., *Physica A*, 2003, **330(3)**, 329.
26 Glavatskiy K.S., *Ph.D. thesis*, Norwegian University of Science and Technology, 2009.
27 Debenedetti P.G., *Metastable Liquids*, Princeton University Press, 1996.
28 Kalikmanov V.I., *Nucleation Theory*, Springer Verlag, 2013.
29 Johannessen E. Bedeaux D., *Physica A*, 2006, **370(2)**, 258.
30 Glavatskiy K.S. Bedeaux D., *J. Chem. Phys.*, 2010, **133(14)**, 144709.
31 Glavatskiy K.S. Bedeaux D., *J. Chem. Phys.*, 2014, **140**, 104708.
32 Johannessen E. Bedeaux D., *Physica A*, 2004, **336(4)**, 252.
33 Wilhelmsen Ø. Bedeaux D. Kjelstrup S. Reguera D., *J. Chem. Phys.*, 2014, **140(2)**, 024704.
34 Yang A.J.M. Fleming P.D. Gibbs J.H., *J. Chem. Phys.*, 1976, **64**, 3732.
35 Glavatskiy K.S. Bedeaux D., *Phys. Rev. E*, 2008, **77(6)**, 061101.
36 Simon S.M. Kjelstrup S. Bedeaux D. Hafskjold B., *J. Phys. Chem. B*, 2004, **108**, 7186.
37 Xu J. Kjelstrup S. Bedeaux D. Røsjorde A. Rekvig L., *J. Colloid and Interface Science*, 2006, **299**, 452.
38 Ge J. Kjelstrup S. Bedeaux D. Simon J.M. Rousseau B., *Phys. Rev. E*, 2007, **75**, 061604.
39 Johannessen E. Bedeaux D., *Physica A*, 2003, **330(3)**, 354.
40 Holyst R. Litniewski M., *J. Chem. Phys.*, 2008, **100**, 055701.
41 Gas P. Girardeaux C. Mangelinck D. Portavoce A., *Materials Science and Engineering B*, 2003, **101**, 43.
42 Røsjorde A. Kjelstrup S. Bedeaux D. Hafskjold B., *J. Colloid and Interface Science*, 2001, **240**, 355.
43 Ge, Jialin. Bedeaux, D. Simon, J.M. Kjelstrup, S., *Physica A*, 2007, **385(2)**, 421.
44 D. Browarzik, J. P. M. Trusler, I. G. Economou, J. Ely, C. McCabe, A. Galindo, M. A. Anisimov, M. C. Kroon, E. Lemmon, S. Bottini, E. Brignole, S. Pereda, S. Kjelstrup, D. Bedeaux and S. I. Sandler, *Applied Thermodynamics of Fluids*, The Royal Society of Chemistry, 2010.
45 Holyst R. Litniewski M. Jakubczyk D. Zientara M. Woźniak M., *Soft Matter*, 2013, **9**, 7766.
46 Yang A.J.M, *J. Chem. Phys.*, 1985, **82**, 2082.
47 Y. C.L., *Yaws' Critical Property Data for Chemical Engineers and Chemists*, Knovel, 2012.
48 Reid R.C. Prausnitz J.M. and Pooling B.E., *The properties of Gases and Liquids 4'th edition*, 1987.
49 Taylor R. Krishna R., *Multicomponent Mass Transfer*, Wiley, 1993.
50 Kempers L.J.T.M., *J. Chem. Phys.*, 2001, **115**, 6330.

A Thermophysical properties

To quantitatively capture the physical phenomena and dependencies expected in the bulk phases, it is imperative to have thermophysical models which take properly into account temperature, pressure and composition dependencies. Diffusion coefficients and viscosities of pure gas and liquid components were calculated by second order polynomials in temperature, listed in literature[47]. The Wassilijewa equation with the Mason and Saxena modification was used to predict the thermal conductivity of gas mixtures[48], and the liquid phase thermal conductivity was weighted with the mass fractions. Following recommendations by Taylor and Krishna[49], the gas phase diffusion coefficients were estimated from the method of Fuller et al. in the gas phase, and the method by Wilke and Chang in the liquid phase[48]. Maxwell-Stefan diffusion coefficients were estimated using the thermodynamic correction factors in the gas phase (See[49] for details). The mixture diffusion coefficient in the liquid was further estimated by the method by Vignes[49], based on the diffusion coefficients in infinite dilution calculated by the Wilke-Chang correlation.

The Soret effect, which describes mass diffusion in a temperature gradient follows a fundamentally different mechanism in the liquid-phase than in the gas-phase. In gases, the Soret effect comes mainly from selective collision interaction between the components. In the liquid, the largest effect comes from selective attraction/repulsion between components. Kempers gave approximate expressions for thermal diffusion in liquids which he later elaborated to include gases[50]. We will here use the method by Kempers, but reformulate the Soret effect in terms of the heats of transfer suitable for our framework:

$$\frac{q_i^o}{v_i} - \frac{q_n^o}{v_n} = \left[\frac{h_{\mathrm{res},n}}{v_n} - \frac{h_{\mathrm{res},i}}{v_i}\right] - RT\left[\frac{\alpha_{\mathrm{ig},n}(1-x_n)}{v_n M_{w,n}} - \frac{\alpha_{\mathrm{ig},i}(1-x_i)}{v_i M_{w,i}}\right] \tag{56}$$

Here subscript "res", refers to a residual property, i.e. the deviation from the ideal gas-phase. The advantage of the expression above is that it is not limited to binary mixtures, is valid for both the liquid and the gas phase, and does not contain the derivative of the chemical potential with respect to mole fractions. In addition to the equation above, $\sum_i^{N_c} w_i q_i^o = 0$ due to the Gibbs-Duhems

relation. The heats of transfer are then available for any mixture through a system of linear equations. In particular, for the two-component system:

$$q_1^o = \left[\frac{h_{\mathrm{res},2}}{v_2} - \frac{h_{\mathrm{res},1}}{v_1} - RT\left(\frac{\alpha_{\mathrm{ig},2}x_1}{v_2 M_{w,2}} - \frac{\alpha_{\mathrm{ig},1}x_2}{v_1 M_{w,1}}\right)\right] \cdot \left[\frac{1}{v_1} + \frac{w_1}{v_2 w_2}\right]^{-1} \quad (57)$$

$$q_2^o = -\frac{w_1 q_1^o}{w_2} \quad (58)$$

Here, α_{ig} are the ideal gas thermal diffusion factors, which were set to 0.07 for both components. The equations above give thermal diffusion factors which are considerably larger in the liquid phase than the gas phase, as expected from experiments.

B Numerical values

The amplitudes used for the gradient contribution to the local resistivities are given in Tab. 2.

Table 2 The amplitudes of the gradient terms in the local resistivity profiles, α

	Case	r_{qq}	r_{q1}	r_{11}
Single-component	n	303.46	(-)	(-)
Single-component	g	6.7367	(-)	(-)
Single-component	l	1115.9	(-)	(-)
Two-component	n	406.1565	1.00	19.661
Two-component	g	7.9787	1.00	0.27145
Two-component	l	1498.585	1.00	1.00